metals

MDPI

Article

Influence of Atomizing Gas Pressure on Microstructure and Properties of Nickel Silicide Intended for Additive Manufacturing

Mohammad Ibrahim [1,*], Federico Simone Gobber [2], Christopher Hulme [3], Geir Grasmo [1] and Ragnhild E. Aune [1,4]

[1] Department of Engineering Sciences, University of Agder (UiA), 4630 Kristiansand, Norway; geir.grasmo@uia.no (G.G.); ragnhild.aune@ntnu.no (R.E.A.)
[2] Department of Applied Science and Technology, Politecnico di Torino, 10129 Torino, Italy; federico.gobber@polito.it
[3] Department of Materials Science and Engineering, KTH Royal Institute of Technology, 100 44 Stockholm, Sweden; chrihs@kth.se
[4] Department of Materials Science and Engineering, Norwegian University of Science and Technology (NTNU), 7491 Trondheim, Norway
* Correspondence: mohammad.ibrahim@uia.no

Abstract: Nickel silicides are crucial in advanced technology applications ranging from semiconductor devices to high-temperature materials. Gas atomization is a process that involves the formation of fine liquid droplets and their rapid cooling and solidification to make powder particles. The final microstructure and the properties of the particles are highly sensitive to the gas atomization process parameters. In the present study, gas atomization of NiSi12-wt% was performed at three different pressures (35, 40, and 45 bars) to optimize the particle size distribution for additive manufacturing applications. A comprehensive range of characterization techniques, including scanning electron microscopy, X-ray diffraction, particle size distribution measurements, light optical microscopy, and density measurements, was used to evaluate the microstructural features, phase composition, and density of the produced NiSi12-wt% powders. Higher atomizing gas pressures resulted in a finer particle size distribution due to improved molten droplet breakup, increased satellite formation, and a well-suited particle size distribution for additive manufacturing applications.

Keywords: gas atomization; nickel silicide; additive manufacturing; metal powder; particle size

check for updates

Citation: Ibrahim, M.; Gobber, F.S.; Hulme, C.; Grasmo, G.; Aune, R.E. Influence of Atomizing Gas Pressure on Microstructure and Properties of Nickel Silicide Intended for Additive Manufacturing. *Metals* **2024**, *14*, 930. https://doi.org/10.3390/met14080930

Academic Editor: Chenglong Ma

Received: 24 June 2024
Revised: 7 August 2024
Accepted: 13 August 2024
Published: 15 August 2024

Copyright: © 2024 by the authors. Licensee MDPI, Basel, Switzerland. This article is an open access article distributed under the terms and conditions of the Creative Commons Attribution (CC BY) license (https://creativecommons.org/licenses/by/4.0/).

1. Introduction

Silicides, such as Ni_3Si, have attracted considerable attention from both industry and academia due to their unique combination of electrical, mechanical, and thermal properties, making them highly promising for diverse applications [1,2]. The materials find application across a range of sectors, including semiconductor device manufacturing [3], aerospace for high-temperature structural components [4], and the energy industry [5]. The optimization of their microstructure and properties holds the key to enhancing their performance in these applications and beyond. However, traditional manufacturing techniques like casting and forging, commonly used for metallic alloys, are incompatible with nickel silicides due to their inherent brittleness and lack of ductility [6]. Consequently, alternative manufacturing methods such as additive manufacturing (AM) and cladding have become crucial for shaping nickel silicides into complex geometries and finely tuned components. Such tunability reduces stress and strain during fabrication [7].

Laser-based additive manufacturing (LBAM) and electron-beam additive manufacturing (EBAM) are particularly noteworthy among the various AM techniques. LBAM employs a high-power laser beam to melt and fuse metal powders or wire feedstock layer by layer, building up the desired object. In contrast, EBAM uses a focused electron beam

for the same purpose [8]. Each technique has its unique advantages and disadvantages. EBAM generally has a higher heat input per unit volume per unit time compared to LBAM. This is primarily due to the greater energy and penetration depths of electron beams, which result in larger melt pools and higher thermal gradients during the build process [9]. These thermal gradients can introduce residual stresses for brittle materials like nickel silicide, leading to cracking or delamination. LBAM, on the other hand, offers finer control over the melt pool, resulting in more localized heat input, potentially reducing the thermal gradients and defects in brittle materials. EBAM also requires a high vacuum environment, which can increase costs and pose processing challenges [10]. LBAM can utilize both wire and powder feedstock, with wire-based processes often yielding coarser microstructures compared to powder-based processes, resulting in more brittle components. Achieving fine features or complex geometries may be more challenging with wire feedstock than with powder-based raw material [11,12].

Gas atomization, the formation of fine liquid droplets from a melt stream by high-pressure gas jets, followed by rapid cooling and solidification, is a crucial technique for producing fine powders suitable for AM [13]. Several critical parameters influence the characteristics of the resulting powders. Higher gas pressure tends to produce finer and more spherical particles, while lower pressures can yield coarser and irregularly shaped particles.

The rate at which the liquid metal is introduced into the atomization chamber, the melt flow rate, impacts the size and yield of the resulting powder, with higher flow rates typically leading to smaller powder particles. The design of the atomizing chamber influences the powder shape, size distribution, and degree of powder aggregation or satellite particle formation. Notably, gas-atomized powder particles tend to assume a spherical shape, as the spheroidization time is orders of magnitude shorter than the solidification time. Optimizing these parameters allows for the production of powders tailored to specific size distributions, morphologies, and properties, addressing applications such as AM, powder metallurgy, and thermal spray coatings [14,15].

The optimization step is crucial as each AM technique has specific preferred particle size ranges. For instance, the technique called laser powder bed fusion technique requires a particle size of 10–60 μm [16], while the directed energy deposition (DED) technique can utilize particles ranging from 50 μm to 150 μm, depending on the manufacturer's requirements [17]. Although companies providing 3D printers also offer metal powders with optimized printing parameters, these powders may be more expensive due to the assurance that they will work seamlessly with a specific 3D printer. However, as the use of 3D printing becomes more widespread, the quality of these powders is expected to improve, and prices may decrease to meet the growing demand across various industries [16].

Various density measures play a crucial role in characterizing metal powders for AM. The apparent density, a straightforward metric obtained by dividing the mass of a sample by its volume, is, for example, vital for bed formation and powder flowability [18]. In the context of AM, the primary objective is to utilize fully dense powders, ensuring effective fusion during manufacturing to produce components with a controlled porosity. True density or skeletal density [19], measured using a helium (He) pycnometer, is also a valuable parameter for assessing powder quality and can be compared against the theoretical density to provide insights into particle porosity. These density considerations are vital for achieving the desired properties and performance in the final AM components. Additionally, understanding and optimizing the particle size and density characteristics are integral steps toward advancing the use of nickel silicides and other advanced materials in AM applications and will be the main focus of the present study.

2. Materials and Characterization

The raw materials, nickel (in the form of crowns from Nikkelverk, Glencore (Kristiansand, Norway), with 99.8% purity), and silicon (sourced from REC Solar (Singapore), with 99.995% purity) were provided by ELKEM Silicon AS, Kristiansand, Norway. The careful selection of high-purity raw materials is essential to avoid impurities that could

compromise the final properties of the alloy. These materials were melted in a 75 kW induction furnace, maintaining a precise composition of 88 wt% Ni and 12 wt% Si. This specific composition is crucial as it aligns with the desired properties of Ni_3Si, making it suitable for applications in which a balance of electrical, mechanical, and thermal properties is essential.

The melting process involved stirring the molten materials with a graphite rod, ensuring thorough mixing. The induction currents played a crucial role in stirring and homogenizing the melts, preventing segregation. Subsequently, the molten alloy was cast into sheets with roughly 10 mm thickness. This step is fundamental in creating a form that can be further processed into the desired powder morphology for AM. Once cooled to room temperature, these sheets were cut into smaller pieces, as shown in Figure 1.

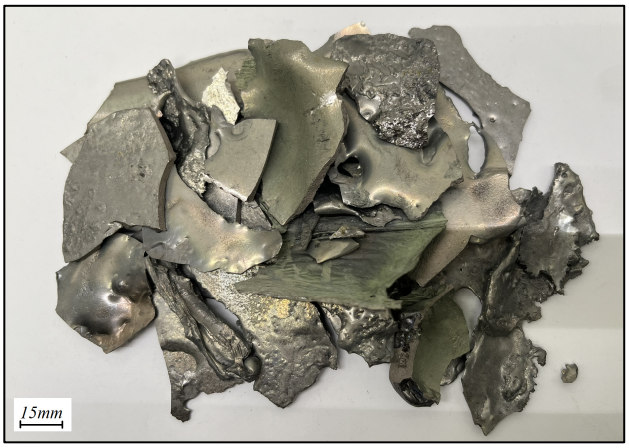


Figure 1. Macroscopic image of NiSi12-wt% pieces intended for gas atomization.

The next phase of the process was carried out at the Polytechnic of Turin, Italy, where batches of powder particles were produced using a closed-coupled atomizer. This closed-coupled type of atomizer, equipped with an annular jet nozzle, is a sophisticated tool for transforming molten alloys into finely atomized powders. Each experimental run involved approximately 5 kg of the alloy undergoing induction heating above its liquidus temperature within an alumina crucible. After loading the crucible with the raw material, both the melt and the atomization chambers were evacuated down to 6×10^{-3} mbar, and the loaded material was heated at approximately 18 ± 2 °C/min by induction heating. The vacuum ensured metal outgassing during the heating stage, but it was backfilled with argon gas (Ar (g)) at approximately 900 °C just before the alloy started melting. The use of Ar (g) serves multiple purposes, including preventing oxidation of the molten metal and creating a controlled atmosphere during the atomization process.

A melt overheat (ΔT) of 150–200 °C was applied to facilitate the heating process. An overpressure of 0.03 mbar was also introduced at the top of the melting chamber. This overpressure was crucial to overcome the melt flow resistance into the nozzle. Maintaining a vacuum during heating was essential to ensure outgassing. Simultaneously, both chambers were filled with argon gas at a temperature of 900 °C. The use of argon serves multiple purposes, including preventing oxidation of the molten metal and creating a controlled atmosphere with known thermal and aerodynamic properties during the atomization process.

A melt delivery tube, constructed from alumina with an inner diameter of 2.5 mm, played a critical role in ensuring the continuous flow of the molten alloy during atomization. This precautionary measure prevented premature solidification of the molten metal, allowing for a smooth and uninterrupted atomization process. The atomization process was initiated by pulling the stopper rod upward, starting the flow of molten metal. A gas flow from the annular jet nozzle impinged upon the molten metal stream after it emerged from the tube and broke it into fine droplets.

Around 90% of the powder was collected in the main collection bottle. The remaining fine particles (having a D50 of 20–25 µm) were collected separately via a cyclone. It is worth noting that the characterization focus was on the powder collected in the main bottle, as the very fine powder particles collected via the cyclone were too small for AM.

The gas atomization parameters outlined in Table 1 provide a comprehensive overview of the conditions during the production of the NiSi12-wt% powders.

Table 1. Gas atomization parameters for the production of NiSi12-wt% powders.

Parameter	NiSi12-wt% (35 bar)	NiSi12-wt% (40 bar)	NiSi12-wt% (45 bar)
Atomizing gas pressure (bar)	35	40	45
Gas mass flow rate (kg/min)	2.18	2.28	2.57
Material loaded (kg)	6.156	6.249	6.149
Melt flow rate (kg/min)	1.92	1.26	1.43
Atomizing chamber pressure (mbar)	1.26	1.28	1.25
Guide tube heating (W)	113.6	115.6	114.2
Melt temperature (°C)	1400–1456	1402–1447	1400–1450

The apparent density of the NiSi12-wt% powder fractions (35, 40, and 45 bar) was evaluated from samples that had passed through a Hall flow funnel and filled a 25 cm^3 container in compliance with ASTM B212 [20]. Five repeated measurements were conducted to ensure accuracy and consistency.

The true density of the powders was determined using a pycnometer from Micromeritics (Model: AccuPyc II 1340, Norcross, GA, USA), operating on gas displacement principles in compliance with ASTM B923 [19]. This method involves measuring the change in pressure pre- and post-gas expansion, allowing for the determination of the powder's volume. Ten measurements were conducted on each powder specimen to ensure reliability.

The morphology and size distribution of the NiSi12-wt% powders were examined using a low-voltage field-emission scanning electron microscope (SEM, Supra 55VP, Zeiss, Oberkochen, Germany), coupled with energy-dispersive spectrometry (EDS) from EDAX (Model: Pleasanton, CA, USA). The SEM, calibrated using a Pelcotec CDMS-1T traceable mount standard (Redding, CA, USA), operated in secondary electron (SE) mode at a 15.0 keV accelerating voltage and a working distance of 10 mm. The EDS analyses were performed to identify the phases present in the sample, providing complementary information to the X-ray diffraction (XRD) findings.

Optical microscopy was performed using a Zeiss Axio Vert.A1 inverted light microscope (Carl Zeiss Microscopy GmbH, Köln, Germany) equipped with an AxioCam MRC Zeiss camera at various magnifications. The images were stored digitally using the Zen Core 3.2 software. The macroscopic observations provide insights into the microscopic features of the NiSi12-wt% pieces meant for gas atomization. Micrographs were also captured using a Wild Heerbrugg Photo Makroskop (Model: M420, Wild Heerbrugg Ltd., Gais, Switzerland) with a Zeiss AxioCam 105 Color digital camera and Zen Core 2.4 software.

For qualitative crystalline phase analysis, an XRD diffractometer (DaVinci D8 Advance, Bruker AXS GMBH, Karlsruhe, Germany) unit with Cu-Kα radiation, a voltage of 40.0 kV, and a current of 30.0 mA was employed. The diffractometer readings were calibrated using a standard reference material, NIST-SRM-660a LaB_6 (Merck-Life Science, Darmstadt, Germany). This calibration involved measuring the standard material to benchmark the diffractometer's readings, particularly the 2θ values from the XRD pattern, against the certified values provided with the reference material. The XRD scan ranged from 10° to 100°, ensuring wide coverage of potential diffraction angles at a steady rate of 2° per minute. Spectral analysis was performed using the Bruker AXS DIFFRAC.SUITE software (specifically the EVA module version 6.0).

The particle size distributions (PSDs) of the NiSi12-wt% powders were meticulously measured using a laser diffraction particle size analyzer (Patrica LA-960, Horiba, Osaka, Japan). The measurements were conducted using the laser-scattering method. To ensure the homogeneity of the samples, a rotation process was used before analysis, i.e., the sample container was inverted and reverted ten times, ensuring that the powder specimen extracted for study was representative of the entire sample. A small quantity of each NiSi12-wt% powder sample, with a refractive index of 2.50, was poured into deionized water with a refractive index of 1.333. The two-step agitation process ensured uniform dispersion and the removal of air bubbles that could interfere with the measurements. The measurements were repeated five times consecutively to ensure consistency in the results.

The sampling and experimental procedures presented serve as a foundation for informed decision-making in the AM process, fostering the development of high-quality components with tailored properties.

3. Results and Discussion

The present study investigating the gas atomization of the NiSi12-wt% alloy specifically explores the influence of atomizing gas pressure on the particle size, morphology, and microstructure. To provide a comprehensive understanding, Figure 2 visually illustrates the initial observations of the atomized powder produced using different atomization gas pressures (35, 40, and 45 bar).

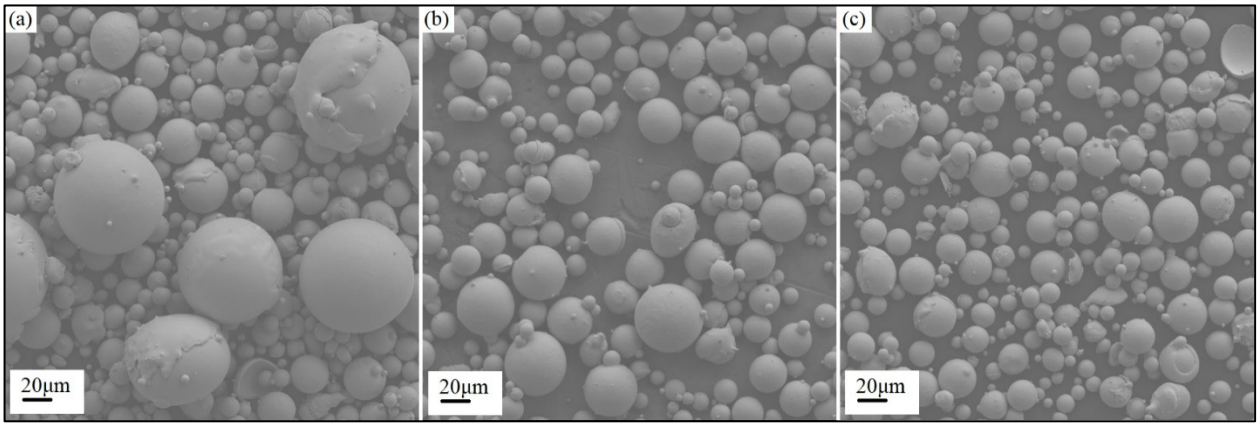


Figure 2. SEM micrographs of gas-atomized NiSi12-wt% powders after sieving through a 125-micron sieve. Powders produced at (**a**) 35 bar atomization gas pressure, (**b**) 40 bar atomization gas pressure, and (**c**) 45 bar atomization gas pressure.

According to the analysis of the SEM images shown in Figure 2, it is evident that there exists an inverse relationship between the atomizing gas pressure and the particle size. This trend can be explained by considering the dynamics of the gas atomization process. Elevated pressures lead to increased kinetic energy of the atomizing gas, which can impart greater force onto the molten metal stream and drive the formation of more surface area in the droplets. This facilitates the breakdown of the molten metal into finer droplets, ultimately yielding powders composed of smaller particles. The SEM images support the inverse correlation between atomizing gas pressure and particle size.

Upon increasing the atomizing gas pressure to 45 bar, a consequential increase in the formation of satellite particles (smaller particles adhering to the surface of larger primary particles during atomization) was evident. The SEM image in Figure 2c clearly illustrates this phenomenon, providing a clear representation of the particle size distribution under varying pressures. Satellite particles are typically generated when high atomizing pressures create smaller droplets, turbulent eddies, and recirculation zones in which the local gas flow is in the opposite direction to the overall flow. Due to their reduced mass and inertia, these smaller droplets are more susceptible to deviating from their path and attaching to larger particles that have not solidified yet [21]. Furthermore, the smaller droplets cool

and solidify faster than large particles and so may solidify before they collide with larger particles, which prevents them from combining to form a single spherical droplet.

This increase in satellite formation significantly reduces the powder's flowability as it creates an irregular and non-uniform particle shape distribution. These irregular shapes result in increased particle interlocking and friction, limiting powder flow. Powder flowability is a critical parameter for various applications, particularly in processes such as powder bed fusion (PBF), in which a consistent and smooth powder flow is essential for creating layers of uniform thickness and density [22].

3.1. Microstructure Analysis

It was observed through LOM and SEM that the microstructure of these powders, regardless of the atomizing gas pressure, was highly dependent on the particle size, exhibiting distinct characteristics for larger and smaller particles. Larger particles generated through this technique showed a predominantly dendritic microstructure. This unique structure can be attributed to the slower cooling rates experienced during the atomization process, allowing for the progressive and directional growth of dendrites from the nucleation site [23]. On the other hand, smaller particles predominantly exhibit an equiaxed microstructure, where grains are approximately equal in dimension along all axes, resulting in a more uniform and isotropic structure. The rapid cooling rates experienced during gas atomization promote the nucleation of new grains throughout the material and limit the time available for atomic diffusion around the solidification front, which is necessary for dendrite formation. Consequently, equiaxed grains are formed, resulting in a fine and uniform microstructure that enhances the material's ductility and toughness [24].

At 35 bar atomization gas pressure, the process yielded particles with a predominantly spherical morphology, but the particle size range was large. Due to insufficient gas pressure, the spherical droplets formed during atomization did not possess the necessary momentum to collide with the walls of the atomizing chamber before they solidified. Consequently, the obtained particles exhibited a well-defined spherical shape and, due to the lower kinetic energy in the gas, were larger. This can also be observed by looking at the much higher melt flow rate values in Table 1 compared to the other two batches. The melt flow rate determines the volume of molten metal that is exposed to the atomizing gas at any given time. A higher melt flow rate means that more molten metal was introduced into the atomization chamber. When the melt flow rate was high, larger molten metal droplets were typically formed as the atomizing gas may not have had sufficient energy or time to break up the larger volume of molten metal into smaller droplets effectively [25,26]. Notably, the absence of splats in this sample emphasizes that the droplets remained suspended until solidification and did not undergo deformation upon contact with the chamber walls.

With an increase in atomization gas pressure to 40 bar, there was a noticeable change in the atomization dynamics. The elevated pressure led to a broadening of the atomization plume, driving the droplets toward the chamber walls with greater force. As these droplets made contact with the walls while still molten, they flattened and solidified, forming larger splats, as shown in Figure 3a. This phenomenon indicates that, while the increased atomization gas pressure somewhat broke down the droplets, they were still of a sizeable diameter upon impact, resulting in more substantial splats. This wide size range of the produced powder particles at 40 bar atomization gas pressure was also reflected in the slightly higher apparent density of these powders, as a wide size distribution is more effective [27]. Upon increasing the atomization gas pressure to 45 bar, the pronounced gas pressure effectively disintegrated the melt stream into finer droplets before it could reach the chamber walls. As these smaller droplets collided with the walls, they formed splats. However, due to their reduced size, the splats were noticeably smaller in diameter compared to the samples produced at 40 bar; see Figure 3b. The visible increase in the number of splats sieved away, coupled with their reduced size, suggests an enhanced atomization efficiency at this elevated atomization gas pressure, along with larger plume formation during atomization.

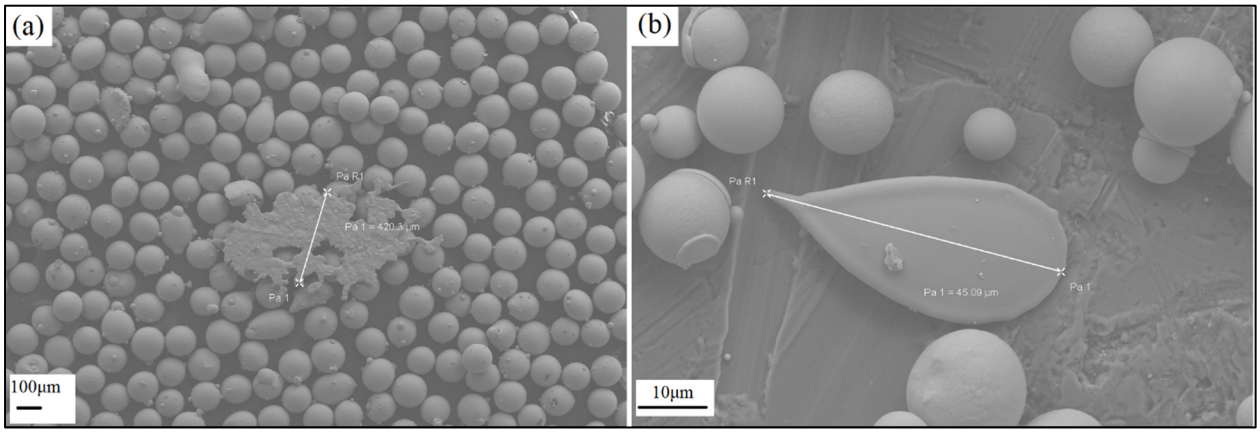


Figure 3. SEM micrographs of NiSi12-wt% powders where splats were produced during the gas atomization at (**a**) 40 bar atomization gas pressure and (**b**) 45 bar atomization gas pressure.

3.2. Density Analysis

Since the main differentiating factor among the three batches of the NiSi12-wt% powders in terms of characteristics was the particle size, the true density values proved to be quite similar for all samples; see Table 2. The true density values refer to the density of the material itself, excluding any pores, voids, or spaces between the particles, and are a fundamental material property that is not influenced by the particle size, shape, or distribution. Apparent density, however, can be affected by these factors. For instance, finer particles might pack more closely together than coarser particles, leading to a higher apparent density. However, very fine powders might have more air entrapped between the particles, leading to a lower apparent density.

The higher frequency of splat powder produced at 40 bar pressure is the reason for the higher apparent density in this powder. Perfectly spherical particles tend to have higher void fractions between them due to their shape, leading to less efficient packing. Due to the higher void fraction, spherical particles typically exhibit lower apparent density compared to irregularly shaped or splat particles. The elongated, flattened shapes of splat particles reduce the voids between them, leading to a denser packing structure.

Table 2. Apparent and true (pycnometric) densities of NiSi12-wt% powders produced at 35, 40, and 45 bar atomizing gas pressure.

Sample	Apparent Density (g/cm^{-3})	True (Pycnometer) Density (g/cm^{-3})
NiSi12-wt% at 35 bar	4.97 ± 0.018	7.7880 ± 0.0011
NiSi12-wt% at 40 bar	5.06 ± 0.016	7.7975 ± 0.0019
NiSi12-wt% at 45 bar	4.93 ± 0.017	7.7815 ± 0.0004

3.3. Splat Formation and Particle Size Distribution

As mentioned earlier, larger splats were found in the NiSi12-wt% powder sample produced with an atomization gas pressure of 40 bar. This resulted in a wider particle size distribution of the powders collected from the main collection chamber (excluding the fines collected using a cyclone), as shown in Figure 4a. Powders with a wider particle size distribution tend to have a higher apparent density as the smaller particles fill the gaps between the larger particles, leading to a more compact arrangement. This is also visible in Table 2 in the apparent density values for the powders produced with an atomization gas pressure of 40 bar. The particle size distribution analyses were even performed after sieving to remove the particle fraction larger than 125 µm, and they showed a clear trend toward a decrease in particle size as the atomization gas pressure was increased; see Figure 4b.

As can be seen from the figure, sieving shortened the PSD by eliminating the tail end that represented the coarser particles.

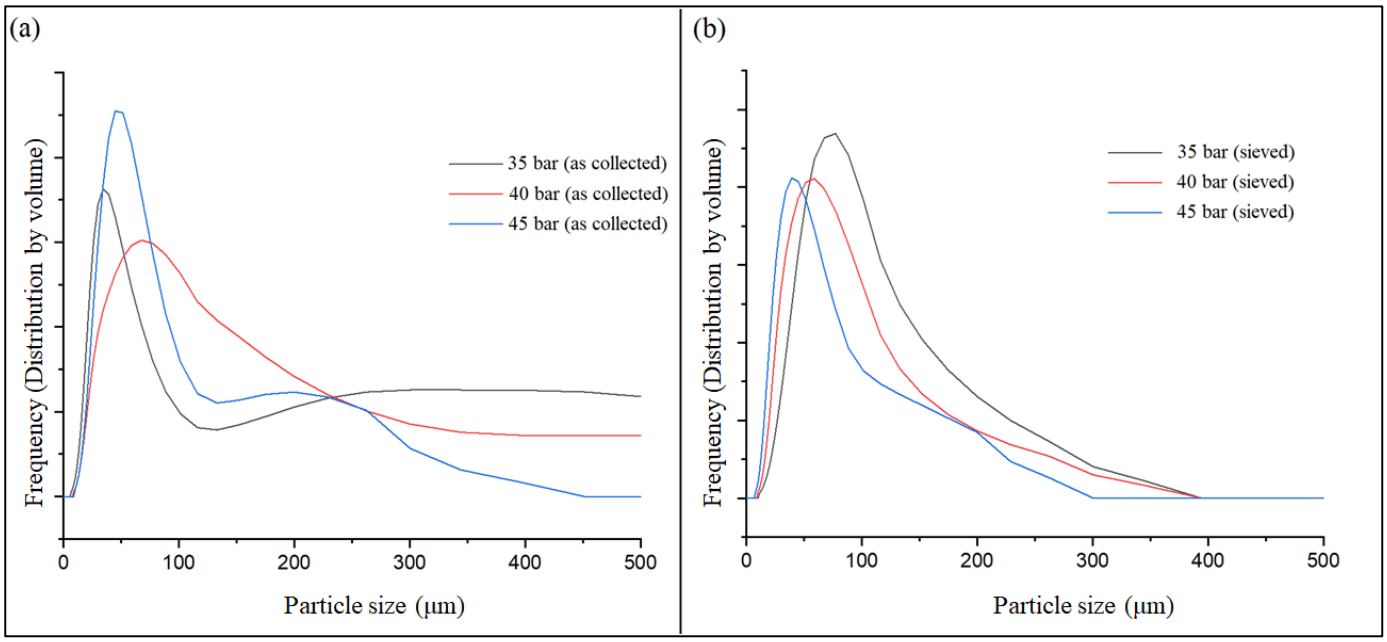


Figure 4. Particle size distribution of the produced NiSi12-wt% powders (**a**) as collected from the atomizer and (**b**) after sieving through a 125 µm sieve, where the black line represents the powder produced with an atomization gas pressure of 35 bar, the red line of 40 bar, and the blue line of 45 bar.

3.4. X-ray Diffraction (XRD) Analysis

The XRD analysis of all three batches of NiSi12-wt% powders produced revealed a unique phase configuration. The scans shown in Figure 5 identify the presence of two predominant phases, i.e., the nickel solid solution and the metastable $Ni_{25}Si_9$ phase [28], in the three powders, which show similar compositions. The appearance of these two distinct phases can be closely linked to the dynamic conditions of the gas atomization process. The cubic Ni phase is recognized as a stable phase, often observed in nickel-based alloys. This phase has a face-centered cubic (FCC) structure, providing the alloy with ductility and flexibility. Silicon atoms are dissolved into the nickel lattice as solute atoms, occupying interstitial or substitutional positions without changing the FCC structure. If observed carefully, the nickel peaks appear to be shifted slightly to the right side of the documented nickel diffraction pattern, which is believed to be an effect of a smaller atom than nickel, such as silicon, substituting it in the solid solution. This causes a contraction of the crystal lattice, which results in diffraction peaks appearing at higher Bragg angles. [29]. On the other hand, the $Ni_{25}Si_9$ phase is a metastable phase that prominently forms under rapid cooling conditions. The high cooling rates during gas atomization clearly led to non-equilibrium solidification, promoting the nucleation and growth of metastable phases like $Ni_{25}Si_9$. In the literature, it has been reported that the $Ni_{25}Si_9$ phase undergoes decomposition at temperatures around 517 °C (790 K) [30]. It is important to consider this when working with nickel–silicon powders produced through gas atomization for AM, as it directly influences the thermal stability of the printed parts and, thereby, their performance under elevated temperatures.

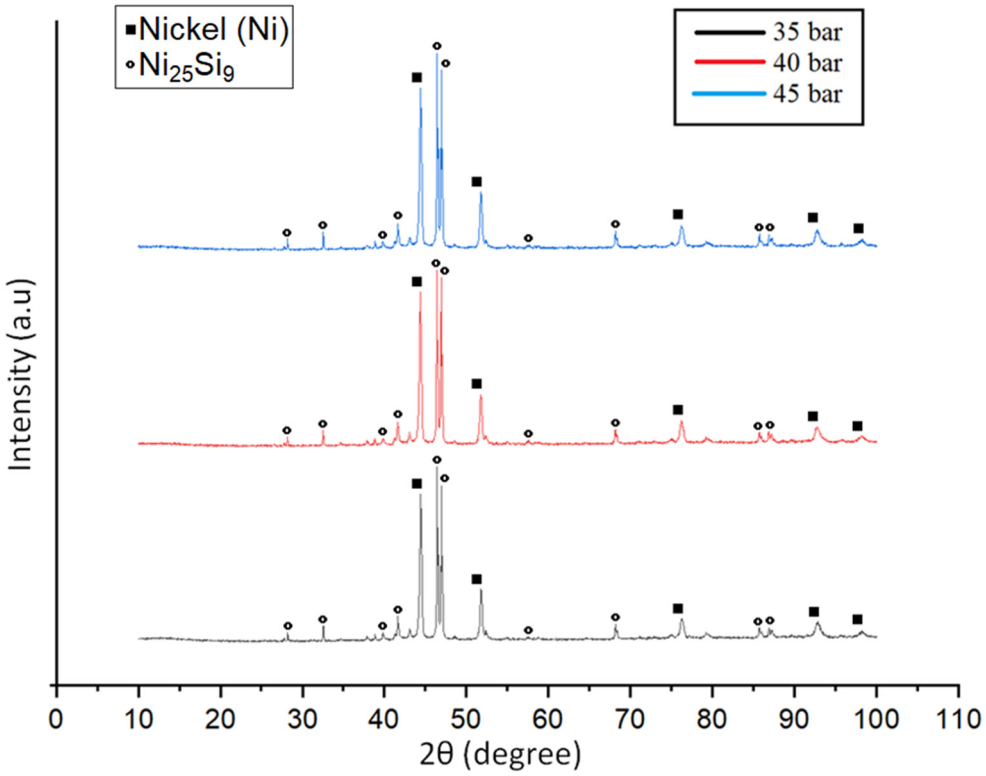


Figure 5. XRD scans of the NiSi12-wt% powders where the black line represents the powder produced with an atomization gas pressure of 35 bar, the red line at 40 bar, and the blue line at 45 bar.

3.5. Comparison with Directed Energy Deposition (DED) Printing

In Figure 6, the micrographs of (i) a cast NiSi12-wt% alloy, (ii) gas-atomized NiSi12-wt% particles, (iii) a NiSi12-wt% DED printed surface, and (iv) the porosity in NiSi12-wt% powders are shown. As can be seen from Figure 6a, large grains were formed during the cooling of the casted sheets in air. The slow cooling gave the atoms more time to migrate and join existing grains, leading to grain growth. The grains in a cast alloy are often dendritic. This dendritic growth results from the constitutional undercooling during solidification, in which the solid phase grows into the liquid phase. Gas atomization, however, involves rapid solidification, which typically results in the formation of much finer grains compared to casting. The rapid cooling rate does not allow the atoms much time to migrate, leading to the nucleation of many small grains without chemical segregation. This phenomenon can be seen in Figure 6b, where equiaxed phases of nickel solid solution are identified alongside the metastable $Ni_{25}Si_9$ phase. For this structure to appear, the $Ni_{25}Si_9$ metastable phase would have had to decompose at high temperatures, leading to a redistribution of the nickel and silicon atoms. This, in turn, would cause the evolution of new phases or the enrichment of the existing nickel solid solution matrix.

The same powder was also used in the DED printing of the alloy [31], which involves localized melting and rapid solidification. The grain size can vary based on the specific process parameters, but it is generally finer than cast alloys and can be comparable to or even finer than gas-atomized powders, especially in the melt pool boundaries, as shown in Figure 6c. As can be seen, the obtained grains were columnar/dendritic in the build direction due to the directional heat flow during the layer-by-layer deposition process.

Cross-sectional analyses were also performed, which revealed the presence of porosity in the powder particles in the form of cavities, as shown in Figure 6d. During the rapid solidification process characteristic of gas atomization, the gas becomes entrapped within the molten droplets. As these droplets solidified, the entrapped gas is unable to escape, leading to the formation of internal pores. Such entrainment reflects the dynamic interaction between the atomization gas velocity, the cooling rate, and the viscosity of the molten

material. Porosity can lead to a reduction in the mechanical strength and toughness of the printed parts as the pores can act as stress concentrators, making the parts more susceptible to fatigue and fracture under load [32].

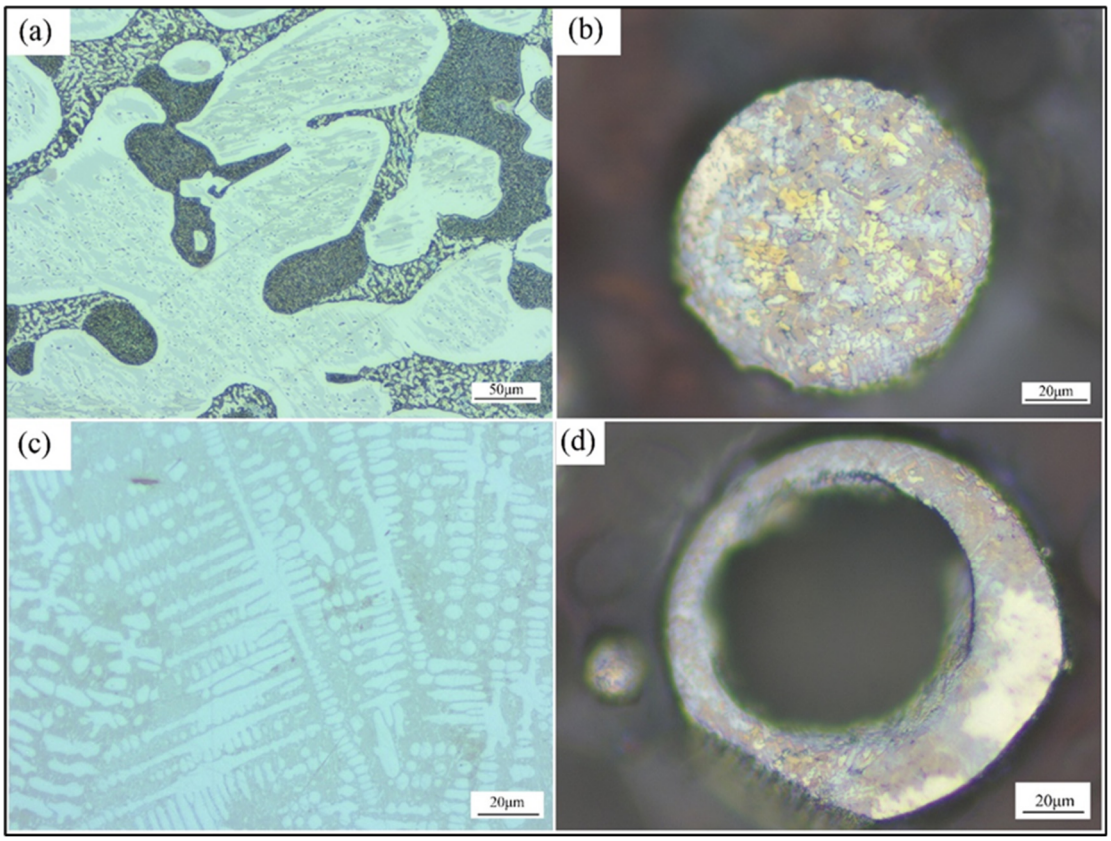


Figure 6. LOM images of the microstructure of (**a**) a cast NiSi12-wt% alloy, (**b**) gas-atomized NiSi12-wt% particles (35 bar), (**c**) the NiSi12-wt% printed surface based on the DED technique, and (**d**) powder porosity as a result of gas entrapment in the NiSi12-wt% powders.

4. Conclusions

The gas pressure used in the gas atomization process is a critical factor in shaping the morphology and size distribution of the resulting NiSi12-wt% alloy powder. Through systematic adjustments in gas pressure, it becomes possible to tailor the powder characteristics, ranging from larger, well-defined spheres to smaller, more numerous splats.

Interestingly, despite the variations in atomization gas pressures, the chemical composition and the phase constitution of the nickel silicide powders remained rather consistent. Detailed SEM and LOM analyses revealed a clear inverse relationship between the atomizing gas pressure and the particle size. Higher pressures lead to increased kinetic energy, promoting the breakdown of molten metal into finer droplets, yielding powders with smaller particles.

An additional noteworthy observation is the increase in satellite particle formation at an atomization gas pressure of 45 bar, which impacts the powder's flowability. The irregular and non-uniform particle shape distribution hindered close particle packing, resulting in a less predictable powder flow. The microstructure analysis indicated size-dependent characteristics, with larger particles exhibiting a predominantly dendritic microstructure and smaller particles displaying an equiaxed microstructure, enhancing ductility and toughness.

The apparent density values obtained in the present study align well with the particle size differences and distribution, especially in view of the presence of larger splats in the 40 bar sample, which influenced the overall powder density. The XRD scans revealed two predominant phases, i.e., the nickel-based solid solution phase and the metastable $Ni_{25}Si_9$

phase. This unique phase configuration, influenced by rapid cooling during gas atomization, highlights the importance of understanding the thermal stability of these powders.

5. Future Work

Given the outcomes and implications of the present study, several areas exist for future research to explore. Differential scanning calorimetry (DSC) can be employed to investigate the melting behavior of the gas-atomized powders. This analytical technique will provide comprehensive insights into the thermal phase transitions and characteristics of the powders under varying thermal conditions. Furthermore, the DSC analysis will also shed light on the decomposition kinetics of the metastable phases present within the powders, offering valuable information on their thermal stability and transformation mechanisms.

There is a need for a thorough investigation into the possibility of oxide formation on the powder surface using X-ray photoelectron spectroscopy (XPS) analysis. Subsequent studies can examine the impact of this oxide formation on the printability and porosity development in components fabricated using these powders.

The suggested future investigations aim to enhance the fundamental understanding of gas-atomized powders and provide practical insights that can guide their optimization for AM applications.

Author Contributions: Conceptualization, M.I.; Methodology, F.S.G., C.H. and R.E.A.; Formal analysis, M.I.; Writing—original draft, M.I.; Writing—review and editing, F.S.G., C.H., G.G. and R.E.A.; Supervision, R.E.A., C.H. and G.G.; Funding acquisition, R.E.A. and G.G. All authors have read and agreed to the published version of the manuscript.

Funding: This research was funded by Norges Forskningsråd, grant number 309856.

Data Availability Statement: The original contributions presented in this study are included in the article; further inquiries can be directed to the corresponding author.

Acknowledgments: The authors gratefully acknowledge the Norwegian Research Council (NFR) for funding the project "Development and Production of Metal Alloys for Powder-Based Additive Manufacturing (MADAM)," Ref. No. 309856, which made the present research possible. They also thank Future Materials—Norwegian Catapult in Grimstad, Norway, and the Department of Material Science and Engineering at the Norwegian University of Science and Technology (NTNU) in Trondheim, Norway, for facilitating the necessary analytical equipment. Special thanks are extended to Jan Ove Odden from Elkem Silicon in Kristiansand, Norway, for providing an opportunity for one of the authors to acquire hands-on training in the gas atomization technique from Marco Actis Grande at the University of Turin in Turin, Italy. His generous hospitality, guidance, and expertise have contributed to the success of the present research activities.

Conflicts of Interest: The authors declare no conflicts of interest.

References

1. Sukidi, N.; Koch, C.C.; Liu, C. The Oxidation of Ni3Si-base Alloys. *Mater. Sci. Eng. A* **1995**, *191*, 223–231. [CrossRef]
2. Cao, Y.; Zhu, J.; Liu, Y.; Nong, Z.; Lai, Z. First-Principles Studies of the Structural, Elastic, Electronic, and Thermal Properties of Ni_3Si. *Comput. Mater. Sci.* **2013**, *69*, 40–45. [CrossRef]
3. Pandey, R.K.; Maity, G.; Pathak, S.; Kalita, P.; Dubey, S. New Insights on Ni-Si System for Microelectronics Applications. *Microelectron. Eng.* **2022**, *264*, 111871. [CrossRef]
4. Chen, X.; Zhang, X.; Guo, H.; Wang, F.J. Insights into the Anisotropic, Electronic, and Magnetism Properties of Ternary TM2Si2Ys (TM = Cr, Fe, Co, Ni) Silicides from the First-Principles Calculations. *Chem. Phys. Lett.* **2022**, *802*, 139763. [CrossRef]
5. Schneider, K.; Bauer, R.; Grünling, H. Corrosion and Failure Mechanisms of Coatings for Gas Turbine Applications. *Thin Solid Films* **1978**, *54*, 359–367. [CrossRef]
6. Li, Z.; Schulson, E.M. The Fracture Toughness of a Brittle Nickel Silicide Containing the Ductile Phases Ni (Si) and Ni3Si. *MRS Online Proc. Libr.* **1992**, *288*, 1081–1086. [CrossRef]
7. Örnek, C. Additive Manufacturing—A General Corrosion Perspective. *Corros. Eng. Sci. Technol.* **2018**, *53*, 531–535. [CrossRef]
8. Lewandowski, J.J.; Seifi, M. Metal Additive Manufacturing: A review of Mechanical Properties. *Annu. Rev. Mater. Res.* **2016**, *46*, 151–186. [CrossRef]
9. Rahman, M.S.; Schilling, P.J.; Herrington, P.D.; Chakravarty, U.K. A Comparison of the Thermo-Fluid Properties of Ti-6Al-4V Melt Pools Formed by Laser and Electron-beam Powder-bed Fusion Processes. *J. Eng. Mater. Technol.* **2021**, *143*, 021003. [CrossRef]

10. Tamakloe, S. Laser Additive Manufacturing Technology Achieves 3D-Printed Ni Single Crystals. *MRS Bull.* **2022**, *47*, 887. [CrossRef]
11. Frazier, W.E. Metal Additive Manufacturing: A Review. *J. Mater. Eng. Perform.* **2014**, *23*, 1917–1928. [CrossRef]
12. DebRoy, T.; Wei, H.; Zuback, J.; Mukherjee, T.; Elmer, J.; Milewski, J.; Beese, A.M.; Wilson-Heid, A.; De, A.; Zhang, W. Additive Manufacturing of Metallic Components–Process, Structure and Properties. *Prog. Mater. Sci.* **2018**, *92*, 112–224. [CrossRef]
13. Gibson, I.; Rosen, D.; Stucker, B.; Khorasani, M.; Gibson, I.; Rosen, D.; Stucker, B.; Khorasani, M. Materials for Additive Manufacturing. *Addit. Manuf. Technol.* **2021**, *Third volume*, 379–428. [CrossRef]
14. Goudar, D.M.; Srivastava, V.; Rudrakshi, G. Effect of Atomization Parameters on Size and Morphology of Al-17Si Alloy Powder Produced by Free Fall Atomizer. *Eng. J.* **2017**, *21*, 155–168. [CrossRef]
15. Xu, L.; Zhou, X.; Li, J.; Hu, Y.; Qi, H.; Wen, W.; Du, K.; Ma, Y.; Yu, Y. Numerical Simulations of Molten Breakup Behaviors of a De Laval-type Nozzle, and the Effects of Atomization Parameters on Particle Size Distribution. *Processes* **2020**, *8*, 1027. [CrossRef]
16. Milewski, J.O. *Additive Manufacturing of Metals: From Fundamental Technology to Rocket Nozzles, Medical Implants, and Custom Jewelry*; Springer: Berlin/Heidelberg, Germany, 2017; p. 38.
17. Singh, A.; Kapil, S.; Das, M. A Comprehensive Review of the Methods and Mechanisms for Powder Feedstock Handling in Directed Energy Deposition. *Addit. Manuf. Technol.* **2020**, *35*, 101388. [CrossRef]
18. Saheb, S.H.; Durgam, V.K.; Chandrashekhar, A. A Review on Metal Powders in Additive Manufacturing. In *AIP Conference Proceedings, Proceedings of the Third International Conference on Inventive Material Science Applications: Icima, Coimbatore, India, 18–19 June 2020*; AIP Publishing: Melville, NY, USA, 2020. [CrossRef]
19. *ASTM B923-23*; Standard Test Method for Metal Powder Skeletal Density by Helium or Nitrogen Pycnometry. ASTM International: West Conshohocken, PA, USA, 2016. [CrossRef]
20. *ASTM B212-21*; Standard Test Method for Apparent Density of Free-Flowing Metal Powders Using the Hall Flowmeter Funnel. ASTM International: West Conshohocken, PA, USA, 1999; pp. 89–91. [CrossRef]
21. Özbilen, S. Satellite Formation Mechanism in Gas Atomised Powders. *Powder Metall.* **1999**, *42*, 70–78. [CrossRef]
22. Kiani, P.; Bertoli, U.S.; Dupuy, A.D.; Ma, K.; Schoenung, J.M. A Statistical Analysis of Powder Flowability in Metal Additive Manufacturing. *Adv. Eng. Mater.* **2020**, *22*, 2000022. [CrossRef]
23. Gianoglio, D.; Ciftci, N.; Armstrong, S.; Uhlenwinkel, V.; Battezzati, L. On the Cooling Rate-Microstructure Relationship in Molten Metal Gas Atomization. *Metall. Mater. Trans. A* **2021**, *52*, 3750–3758. [CrossRef]
24. Wang, J.; Yang, H.; Ruan, J.; Wang, Y.; Ji, S. Microstructure and Properties of CoCrNi Medium-Entropy Alloy Produced by Gas Atomization and Spark Plasma Sintering. *J. Mater. Res. Technol.* **2019**, *34*, 2126–2136. [CrossRef]
25. Zhao, X.; Xu, J.; Zhu, X.; Zhang, S. Effect of Atomization Gas Pressure Variation on Gas Flow Field in Supersonic Gas Atomization. *Sci. China Ser. E Technol. Sci.* **2009**, *52*, 3046–3053. [CrossRef]
26. Wang, J.; Xia, M.; Wu, J.; Ge, C. Ladle Nozzle Clogging in Vacuum Induction Melting Gas Atomization: Influence of the Melt Viscosity. *Metall. Mater. Trans. B* **2022**, *53*, 2386–2397. [CrossRef]
27. Heaney, D.F. *Handbook of Metal Injection Molding*, 2nd ed.; Woodhead Publishing: Sawston, UK, 2019; pp. 56–57. [CrossRef]
28. Ibrahim, M.; Du, Q.; Hovig, E.W.; Grasmo, G.; Hulme, C.; Aune, R.E. Gas-Atomized Nickel Silicide Powders Alloyed with Molybdenum, Cobalt, Titanium, Boron, and Vanadium for Additive Manufacturing. *Metals* **2023**, *13*, 1591. [CrossRef]
29. Mahmood, N.B.; Saeed, F.R.; Gbashi, K.R.; Hamodi, A.; Jaffar, Z.M. Structural Properties of $Co_xCu_{1-x}Fe_2O_4$ Solid Solution. *J. Mech. Behav. Mater.* **2021**, *30*, 220–227. [CrossRef]
30. Cao, L.; Cochrane, R.; Mullis, A.M. Microstructural Evolution and Phase Formation in Rapidly Solidified Ni-25.3 At. Pct Si Alloy. *Metall. Mater. Trans. A* **2015**, *46*, 4705–4715. [CrossRef]
31. Ibrahim, M.; Hulme, C.; Grasmo, G.; Aune, R.E. Experimental Evaluation of Microhardness and Pitting Corrosion Resistance of Nickel Silicide (NiSi12-wt.%) Laser Cladded Surfaces. *Materials*, 2024; *submitted*.
32. Chen, G.; Zhao, S.; Tan, P.; Wang, J.; Xiang, C.; Tang, H. A Comparative Study of Ti-6Al-4V Powders for Additive Manufacturing by Gas Atomization, Plasma Rotating Electrode Process and Plasma Atomization. *Powder Technol.* **2018**, *333*, 38–46. [CrossRef]

Disclaimer/Publisher's Note: The statements, opinions and data contained in all publications are solely those of the individual author(s) and contributor(s) and not of MDPI and/or the editor(s). MDPI and/or the editor(s) disclaim responsibility for any injury to people or property resulting from any ideas, methods, instructions or products referred to in the content.